Journal of Materials Chemistry A

PAPER

View Article Online
View Journal | View Issue

Cite this: J. Mater. Chem. A, 2016, 4, 16225

Metal–organic framework-guided growth of Mo_2C embedded in mesoporous carbon as a high-performance and stable electrocatalyst for the hydrogen evolution reaction†

M. Qamar,*[a] A. Adam,[b] B. Merzougui,[c] A. Helal,[a] O. Abdulhamid[a] and M. N. Siddiqui[b]

Received 1st August 2016
Accepted 18th September 2016

DOI: 10.1039/c6ta06553h

www.rsc.org/MaterialsA

Large-scale production of H_2 by electrochemical water splitting is discerned as one of the most economical and viable approaches and designing Pt-less electrocatalysts remains at the forefront of this technology development. Herein, *in situ* transformation of metal–organic frameworks (MOF), impregnated with a molybdenum precursor, into a porous and rigid carbon support and molybdenum carbide (Mo_2C) was demonstrated to fabricate highly active and stable β-Mo_2C/C heterostructure for electrocatalytic H_2 evolution. The two-step synthesis approach involved the impregnation of molybdenum source into frameworks of MOF (namely MIL-53(Al)) followed by nucleation and growth of Mo_2C nanocrystals into confined porous texture through carburization. Characterization revealed the formation of mesoporous carbon embodied with crystalline nanoparticles of β-Mo_2C (between 5 and 10 nm). A probable mechanism for the formation of Mo_2C/C nanocomposite is proposed. The propensity of the catalyst was tested towards the electrocatalytic H_2 evolution reaction (HER) under alkaline aqueous media (1 M KOH). The electrocatalyst showed a remarkable HER activity as compared to the benchmark electrocatalyst Pt/C and Mo_2C/XC72 black catalysts at 10 mA cm^{-2} and stability for 20 h at the same current density. Electrochemical impedance spectroscopy results of Mo_2C/C were construed by two time constants, porosity and charge transfer, and the HER reaction followed the Volmer–Heyrovsky mechanism.

Introduction

The surge in the field of renewable energy aiming to develop clean energy technology is continuing to rise. The quest for an H_2-based economy derived from non-fossil resources remains at the forefront of future fuels. During the past few decades, there has been intense research on the use of electrical energy to produce H_2 in an energy efficient and environmentally benign way.[1–4] Electrocatalytic hydrogen generation *via* water electrolysis provides an important alternative to that extracted from hydrocarbon resources. The technological development of water electrolysis to achieve a high flow rate of hydrogen is essentially decelerated by the requirement of high overvoltage. Development of a catalyst that can lower the overpotential for hydrogen generation is the cost-determining factor of the overall electrocatalytic process. Hence, one of the most crucial components, which could revolutionize H_2 production, is the design and development of a robust electrocatalyst that can efficiently split water at overpotentials as low as possible. Currently, platinum (Pt) is known as a state-of-the art electrocatalyst for the hydrogen evolution reaction (HER) and oxygen reduction reaction (ORR). However, due to high cost and its scarcity, research focus has shifted to precious-metal-free based materials for an efficient HER reaction.[5–7] Consequently, a wide variety of materials consisting of non-precious metals such as metal carbides (Mo_2C,[8–12] WC[13–15]), metal sulfides (MoS_2,[16,17] WS_2,[18,19] and CoSe[20,21]), metal phosphides (Ni_2P & Ni_5P_4,[6,22–26] Cu_3P,[27] and FeP[28–30]), metal nitrides ($Co_{0.6}Mo_{1.4}N_2$,[31] and $NiMoN_x$/C[32]), WO_X–carbon[33] and Ni_3Se_2 nanoforest/Ni foam[34] have been explored.[35–40] A noticeable reduction in the overpotential of several new nonprecious metal electrocatalysts was achieved.[4] To this end, due to the unique d-band electronic structure, the Mo-based electrocatalysts, such as Mo_2C and MoS_2, have been the subject of intense investigation for the electrochemical hydrogen evolution under harsh acidic or basic conditions. Progressively, such electrocatalysts show platinum-like catalytic activity for the HER reaction. Yet, functional and robust catalysts operating with reasonable current densities (J) at low overpotentials in water are scarce.[36–39]

It is generally accepted that achieving control of the architecture and composition of nanoscale materials could lead to

[a]Center of Excellence in Nanotechnology (CENT), King Fahd University of Petroleum and Minerals, Dhahran 31261, Saudi Arabia. E-mail: qamar@kfupm.edu.sa
[b]Department of Chemistry, King Fahd University of Petroleum and Minerals, Dhahran 31261, Saudi Arabia
[c]Qatar Environment & Energy Research Institute, Qatar Foundation, Doha 5825, Qatar

† Electronic supplementary information (ESI) available. See DOI: 10.1039/c6ta06553h

the development of new materials and systems with enhanced physico-chemical properties. The potential for success lies in the appropriate tailoring and engineering of the nanomaterials. Since electrochemical hydrogen evolution is a predominantly surface-dictated phenomenon, the shape, size, interface, porosity (high surface area and active sites) and composition are highly effective factors among others in enhancing the H_2 evolution and decreasing the overpotential. In addition, it has been increasingly documented that the electrocatalytic activity of Mo_2C also depends on the type of carbon support and the extent of dispersion of active sites on its surface. Coupling between active catalysts and support may induce a unique metal–support-interaction which may ultimately influence various phenomena, such as the interfacial equilibrium, adsorption and/or desorption of the reactive species and their interaction with the electrocatalysts surface and electrical conductivity. For instance, Chen *et al.*, demonstrated that Mo_2C supported on carbon nanotubes showed higher activity as compared to that of being supported on carbon black (XC72).[8] Furthermore, Mo_2C/CNT was found to be highly stable under the applied experimental conditions. Similarly, mesoporous graphitic carbon nitride has also been used as a reactive template to prepare molybdenum carbide–carbon nanocomposites for electrochemical hydrogen evolution.[41] In another recent study, Zhang *et al.*, reported the synthesis of porous one-dimensional Mo_2C supported on amorphous carbon as a highly efficient and durable electrocatalyst for hydrogen generation in acidic media.[42] Several examples could be presented here underlining the fact that the carbon support endowed with fairly dispersed active catalysts on the surface played a vital role in determining electrocatalytic activity.

Recently, synthesis of porous molybdenum carbide for electrocatalytic H_2 evolution has been demonstrated using a Cu-based MOF [HKUST-1; $Cu_3(BTC)_2(H_2O)_3$] with Mo-based Keggin-type POMs ($H_3PMo_{12}O_{40}$) (NENU-5) and $Mo_3(BTC)_2$.[9,43] In another recent study, a nickel–carbon-based electrocatalyst was prepared by carbonization of Ni-based metal–organic frameworks followed by electrochemical activation for the HER reaction.[44] MOFs are a relatively new class of materials and their availability with desired metals is limited. Developing an approach to address this gap appeared attractive and significant. Herein, we demonstrate a MOF-steered novel strategy to synthesize β-Mo_2C embedded in porous carbon as an electrocatalyst for the H_2 evolution reaction. This approach was based on the impregnation chemistry; a desired metal source (molybdenum chloride in this case) was dispersed and impregnated in the texture of metal–organic framework (MIL-53(Al)), unlike previous studies in which molybdenum- or Ni-based metal–organic frameworks were synthesized and employed. A microporous matrix in the MIL-53(Al) was used as a confined environment for the guided nucleation and growth of Mo_2C nanocrystallites. The rationale behind using the porous frameworks of MIL-53(Al) was to preclude agglomeration and coalescence of Mo_2C, which are predominant under normal ambience. The catalyst was thoroughly characterized by various techniques and electrocatalytic property for HER reaction was studied. The as-prepared Mo_2C/C nanocomposite showed stable and highly efficient electrocatalytic hydrogen evolution in alkaline (1 M KOH) aqueous media. Furthermore, the electrocatalytic performance of Mo_2C/C was compared with that of commercial electrocatalyst Pt/C and Mo_2C/XC72.

Experimental

Synthesis of metal–organic framework (MIL-53(Al))

Synthesis of MIL-53(Al) was carried out by the hydrothermal method.[45] $Al(NO_3)_3 \cdot 9H_2O$, 1,4-benzenedicarboxylic acid and deionized water were placed in a Teflon-lined steel autoclave and heated at 220 °C for a specific time duration. After completion of the reaction, the resulting white product was filtered, washed with distilled water, dried overnight at 90 °C and activated.

Synthesis of Mo_2C/C electrocatalyst

In a typical synthesis, a predetermined amount of molybdenum source ($MoCl_5$) was dissolved in anhydrous isopropanol and the solution was kept under stirring for 2 h. After complete dissolution of $MoCl_5$, a measured amount of MOF was suspended and kept under stirring for 12 h to ensure complete impregnation of the Mo source into the MOF structure. The weight ratio of Mo : C was adjusted to 40 : 60. As the MIL53(Al) was sensitive towards moisture, the as-synthesized MOF samples were heated at 120 °C overnight and then suspended immediately into the reaction solution to avoid any moisture adsorption, which could affect the molybdenum impregnation and hence the activity. The solvent, isopropanol was then evaporated with vigorous stirring, leaving behind a gel-like product. The resulting product was dried in an oven and finally carburized in a tubular furnace in the presence of CH_4 flow at the desired temperature (with a heating rate of 1.5 °C min^{-1}) for 2 h. The flow of gas was maintained 100 mL min^{-1} with a mass flow controller (Alicat). After the reaction, the black product was collected and subjected to NaOH treatment for Al removal. For Al removal, the product was stirred in a 4.0 M aqueous solution of NaOH and washed thoroughly with deionized water. This process was repeated several times to ensure complete removal of Al. Finally, the obtained product was dried and used as an electrocatalyst for the HER reaction. Mo_2C/XC was synthesized following identical conditions, but XC72 carbon was used instead of MOF as a support.

Characterization

Morphological and detailed microstructural attributes of the materials were discerned with the aid of a field emission scanning electron microscope (FE-SEM, Tescan Lyra-3), transmission and high-resolution transmission electron microscopes and selected area electron diffraction (TEM/HR-TEM, FEI Tecnai TF20) (SAED). Other techniques employed for characterization of the samples were as follows: X-ray diffractometry (XRD, Rigaku MiniFlex), BET surface area analyzer (Micromeritics ChemiSorb 2750), and X-ray photoelectron spectroscopy (XPS, Thermo Scientific ESCALAB 250Xi).

Evaluation of electrocatalytic activity

A suspension consisting of electrocatalyst (10 mg), water and isopropanol (30% v/v) and 37 μL of 1.66 wt% Nafion® was prepared and sonicated for approximately 30 min to obtain a homogeneous ink. A measured amount (16 μL) of the suspension was deposited on a pre-cleaned glassy carbon (GC) disc electrode (5.0 mm diameter, 0.196 cm^2, Pine Instruments) and allowed to dry under air flow at ambient temperature. The deposition steps were repeated to obtain the desired catalyst loading on the GC electrode. The electrocatalytic activity was studied in a three-electrode cell assembly connected to a potentiostat (EG&G 273A). A 1.0 M KOH solution was used as the working electrolyte. A saturated calomel electrode (mercury/mercury chloride, SCE) and coiled platinum mesh were used as the reference and counter electrodes, respectively. Linear sweep voltammetry was applied with a 5 mV s^{-1} scan rate. The SCE electrode was calibrated against the normal hydrogen electrode (NHE) and its potential was converted into the NHE potential. The current density was calculated against the geometric area of the glassy carbon electrode and presented after *iR* correction. Before and during the cathodic measurement, high purity H_2 gas was used to remove the dissolved O_2 from the solution. Electrochemical impedance spectroscopy (EIS) was performed in 1.0 M KOH between the frequency range of 10^5 Hz and 0.01 Hz with AC amplitude of 10 mV. All the EIS data was normalized to the geometric surface area of the working electrode.

Results and discussion

A schematic of the various steps involved in the synthesis of Mo_2C/C is presented in Fig. 1. The metal–organic framework (MIL-53(Al)) was synthesized hydrothermally at 220 °C by heating an aqueous solution of aluminium nitrate and phthalic acid. Furthermore, MIL-53(Al) was suspended in a clear solution consisting of anhydrous isopropanol and molybdenum chloride for homogeneous and uniform impregnation of molybdenum into the MOF frameworks. Care should be taken while adding molybdenum chloride into anhydrous isopropanol as it reacts rapidly with alcohol producing hydrochloric acid. As-prepared MIL-53(Al) was heated at 120 °C to remove adsorbed water or moisture, as it is hygroscopic in nature, and was immediately added into the reaction mixture. Isopropanol was evaporated and produced a molybdenum-enriched MIL-53(Al), which was indicated by a color change from white to dark blue, and subjected to heat treatment to obtain Mo_2C/C. During the carburization process under CH_4 flow at high temperature, MOF (1) provided a limited space for fair dispersion, controlled nucleation and growth of fine Mo_2C nanocrystals and (2) transformed into a mesoporous and rigid carbon support carrying Mo_2C nanoparticles. Restricted and ordered array of microporous texture of MIL53(Al) is likely to inhibit agglomeration and coalescence of Mo_2C nanoparticles, presumably through homogeneous distribution of molybdenum on MOF frameworks (external and internal). Lastly, metallic Al was leached out selectively with highly concentrated aqueous solution of NaOH to produce the desired electrocatalyst. Furthermore, CH_4 acted as a reducing agent and is a prerequisite to obtain Mo_2C/C. Reaction between CH_4 and oxide of metal–organic frameworks could lead to the formation of CO_2 and CO gases. Moreover, decomposition of CH_4 at high temperature could produce H_2 and hydrocarbon gases such as C_2H_2 and C_3H_6. Gas production can act as a reductant and source of carbon. In contrast, formation of molybdenum dioxide (MoO_2) was observed when the molybdenum-impregnated MOF was annealed under N_2 or Ar at 800 °C for 2 h (Fig. S1†).

Formation of MIL-53(Al) was confirmed by XRD and BET analyses. XRD patterns, shown in Fig. 2, indicate typical patterns of MIL-53(Al) that display the crystalline nature of the sample. Furthermore, peaks at approximately 8.7° and 10° are very indicative of a narrow-pore form; upon water/moisture adsorption, the structure of MIL-53(Al) is reported to develop from a large-pore to narrow-pore form.[46] The XRD patterns of the molybdenum-impregnated sample, presented in Fig. 2A, suggest the stability and retention of basic frameworks of MIL-53(Al), except the occurrence of pore size narrowing[46] as indicated by noticeable attenuation in the intensity of peaks at 8.7°

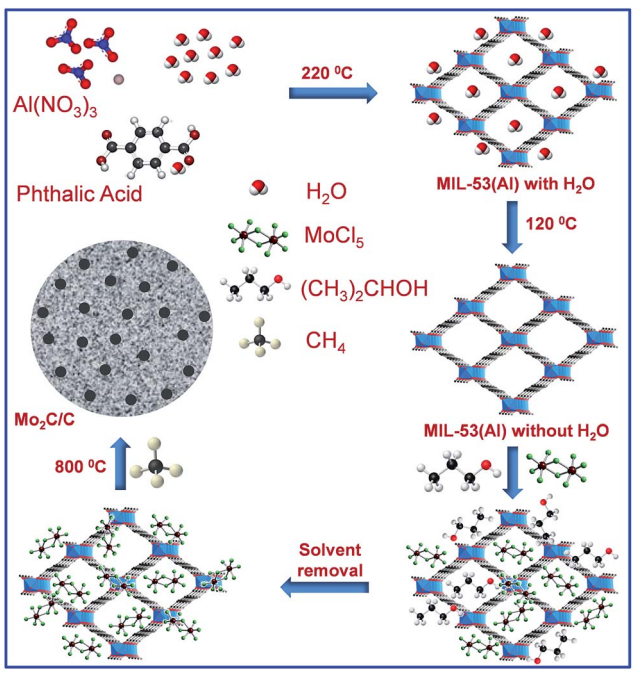

Fig. 1 Schematic of the pathways likely involved in the formation of Mo_2C/C electrocatalyst.

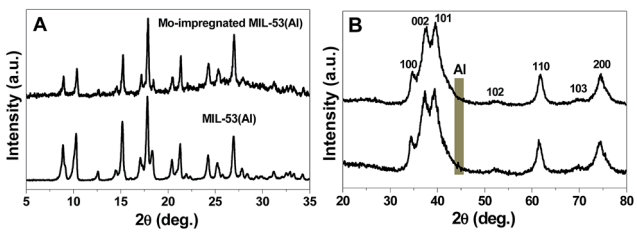

Fig. 2 Powder XRD patterns of (A) MIL-53(Al) before and after molybdenum impregnation, and (B) Mo_2C/C nanocomposite before and after Al removal.

and 10°. However, a drastic change occurred in the structural features after heat treatment at 800 °C or higher temperature under CH_4 flow. Typical XRD patterns of samples obtained after carburization are shown in Fig. 2B. The patterns indicated the formation of a good crystalline structure and the diffraction peaks centred at 34.3° (100), 37.9° (002), 39.4° (101), 52.1° (102), 61.7° (110), 69.6° (103), and 74.5° (200) are attributed to the β-Mo_2C phase with a hexagonal closed packed structure (PDF-00-001-1188).[47] XRD analysis of annealed samples also suggested formation of the β-Mo_2C phase with improved crystallinity. Moreover, aluminium was observed in the XRD analysis, as MIL-53(Al) contains aluminium. It was removed from the nanocomposite through alkaline treatment using highly concentrated NaOH solution. Absence of an aluminium diffraction peak in the XRD spectra indicated that Al was completely leached out without affecting the crystal structure of the Mo_2C/C nanocomposite. Removal of Al was confirmed by XPS analysis, as shown in Fig. S2.†

BET study (Fig. S3A†) verified the microporous texture of MIL-53(Al). The nitrogen adsorption–desorption isotherms of the synthesized MIL-53(Al) presented type-I adsorption and desorption curves with a BET surface area of 1165 $m^2\ g^{-1}$. Similar isotherms for MIL-53(Al) are documented in the literature.[46,48] Interestingly, MIL-53(Al) containing a molybdenum metal source heated at 800 °C under methane showed a transformation from microporous to mesoporous texture (Fig. S3B†). As shown, the N_2 adsorption–desorption isotherms conformed to the classical type-IV behavior that is characteristic of mesoporous materials. A narrow pore size distribution centred at ~3.6 nm was observed (inset figure in Fig. S3B†).

The FE-SEM and TEM images shown in Fig. 3 highlight the size, morphology, and homogeneity of Mo_2C/C. The FE-SEM image showed that the Mo_2C/C nanocomposite possessed irregular and ill-defined morphology, closely resembling to the shape and morphology of the as-prepared MIL-53(Al). Further structural details and distribution of Mo_2C nanocrystallites were analysed by TEM, as shown in Fig. 3B and C. As evident, Mo_2C grains are almost uniform and near-spherical in the 5 to 10 nm size range. The attributes of the carbon layer around the electrocatalyst may have a substantial impact on the electrical conductivity and release of hydrogen bubbles. Fig. 3D reveals that Mo_2C nanoparticles were well-distributed and effectively embedded in the thin layers of carbon with mesoporous feature derived from the carburization of MIL-53(Al) MOF. A localized EDS analysis further corroborated that these thin layers were essentially carbon. The electron diffraction and the HR-TEM microscopy images (Fig. 3E and F) showed the polycrystalline nature of the sample with a high degree of crystallinity. The interplanar distance for the (101) plane was computed to be 0.23 nm, in good agreement with 0.23 nm based on the XRD data. Furthermore, crystal structure, morphological details and distribution of Mo_2C nanoparticles supported on XC carbon were also obtained by XRD and TEM, as shown in Fig. S4.† XRD patterns confirmed the formation of crystalline β-phase of Mo_2C. However, TEM investigation revealed the formation of bigger Mo_2C nanoparticles with particle size in the 20 to 40 nm range. MOF has a porous texture created by organic ligands,

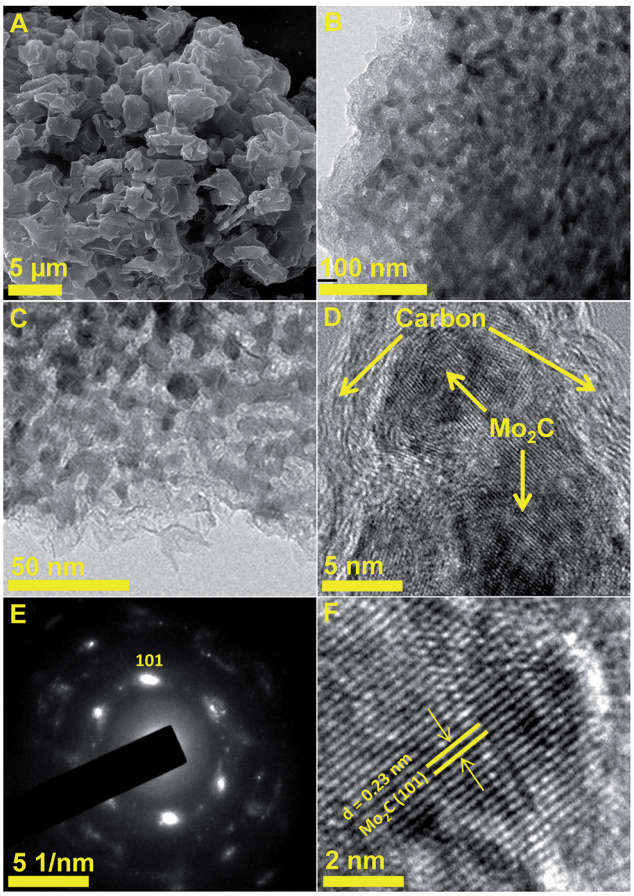

Fig. 3 FESEM, TEM, SAED and HR-TEM of Mo_2C/C.

which are susceptible to heat treatment. At a high temperature such as 800 °C, the microporous structure of MOF collapsed and transformed into mesoporous carbon, which was confirmed by BET analysis. Moreover, at high temperatures, sintering and growth of Mo_2C is likely to take place, thus giving rise to the Mo_2C particles between 5 and 10 nm. However, the growth of Mo_2C was still restricted by the porous texture of MOF or mesoporous carbon. In contrast, when Mo_2C was grown on commercial XC carbon, the particle size was bigger, highlighting the effect of MOF.

Detailed chemical composition and oxidations states of Mo_2C/C were investigated by XPS, and respective spectra for Mo and C, are illustrated in Fig. 4. XPS survey scans before and after

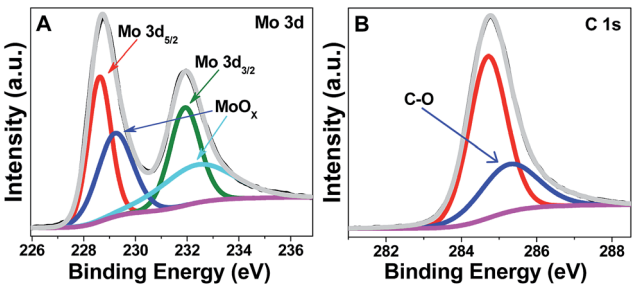

Fig. 4 XPS signatures of Mo_2C/C: (A) Mo 3d and (B) C 1s.

Al removal are shown in Fig. S2,† suggesting removal of Al from Mo_2C/C after alkaline treatment. The binding energy peaks at 228.7 and 231.8 eV were attributed to the Mo $3d_{5/2}$ and Mo $3d_{3/2}$ of Mo(II) spectral lines, respectively; these are in good agreement with those reported in the literature for Mo_2C.[49,50] In addition, peaks at binding energies of 229.2 and 232.3 eV were observed to be belonging to molybdenum oxide. The surface of Mo_2C was susceptible to oxide (MoO_2 and MoO_3) formation when exposed to an air atmosphere. Formation of oxides has been observed in previous studies.[49,50] In addition to the characteristic peak of graphitic carbon at 284.6 eV, the C 1s spectrum (Fig. 4B) also showed the presence of C–O (at 285.5 eV) groups in the layers of as-prepared Mo_2C/C catalyst.

The reduction of cathodic overpotential for H_2 evolution particularly in alkaline media is of great interest in alkaline water electrolysis cells and during some industrial productions, such as chlor-alkali and chlorate cells.[51] In this study, therefore, the electrocatalytic performance of as-prepared samples was evaluated in 1.0 M KOH solution. The cathodic polarization (current density *vs.* potential) profiles for Mo_2C/C prepared at different annealing temperatures, such as 750, 800, 900, and 1000 °C, are shown in Fig. 5A. The current density was calculated based on the geometric area of the glassy carbon electrode in all results reported herein unless specified otherwise. As can be seen, the activity increased with increase in temperature from 750 °C to 800 °C, followed by a decrease at higher temperature such as 900 °C and 1000 °C. Since electrocatalytic HER reaction is predominantly surface-dictated, it could be governed by various physicochemical features of the catalyst including crystallinity and area of surface, which are primarily determined by the process temperature. XRD diffraction patterns of all the samples were recorded and found to be similar, which suggests the formation of β-Mo_2C nanoparticles, except for the improvement in crystallinity with the increasing process temperature (Fig. S6†).

In addition, BET analysis indicated a substantial drop in the surface area of catalyst after heat treatment and this reduction in the surface area continued with the increasing temperature presumably due to particle sintering at high temperatures. The surface area of MOF was measured to be 1165 $m^2\ g^{-1}$, whereas for Mo_2C/C obtained at different temperatures such as 750, 800, 900, and 1000 °C was 202, 168, 113 and 58 $m^2\ g^{-1}$, respectively. The electrochemical active area of Mo_2C/C annealed at different temperatures was quantified through the measurement of double layer capacitance (C_{dl}) of cyclic voltammograms recorded at different scan rates (Fig. S7†). The highest double layer capacitance (24 mF cm^{-2}) was possessed by the sample prepared at 750 °C, and it decreased with increasing process temperature. Usually, higher C_{dl} is demonstrated as higher electrochemical active area.[9,52,53] Although the sample prepared at 750 °C had the highest C_{dl}, Mo_2C/C synthesized at 800 °C showed better performance. Higher C_{dl} or electrochemical active area could also result from a higher real surface area, and the inferior activity could be attributed to its low crystalline structure, as indicated by XRD. The electrochemical activity could also be represented as a specific activity (mA cm^{-2} real), normalized to the real area of the active materials.

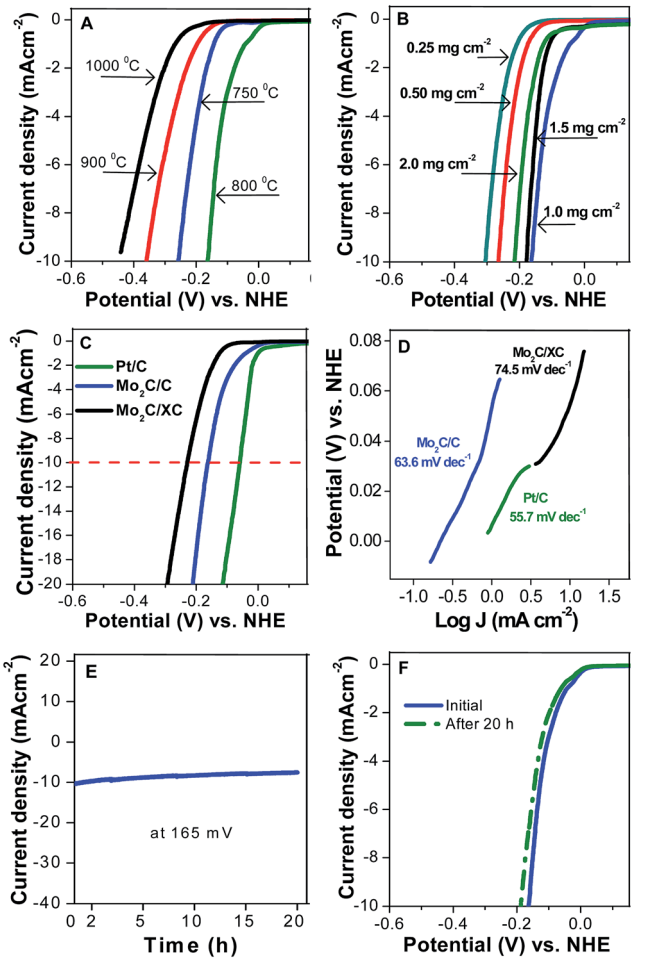

Fig. 5 Potentiodynamic curves showing the effect of carburization temperature (A) and catalyst loading on GCE (B). Comparative current–potential curves of Pt/C, Mo_2C/C and Mo_2C/XC72 (C) and their Tafel plots (D). A time-dependent profile of current density at η = 165 mV for 20 h (E), and polarization curves before and after the durability test (F).

Potentiodynamic curves of specific activity or specific current density calculated with respect to real surface area of Mo_2C/C composite are shown in Fig. S8.† Mo_2C/C prepared at 800 °C showed the highest specific activity, though the real area (168 $m^2\ g^{-1}$) was lower as compared to the sample prepared at 750 °C. The trend of specific current density with respect to temperature agreed well with that of the current density. The higher electrocatalytic activity (with a small overpotential of 165 mV at 10 mA cm^{-2}), shown by samples annealed at 800 °C, appears to be due to an optimal compromise between the surface area and degree of crystallinity. The lower activity at lower temperature (750 °C) could be due to poor degree of crystallinity, which is not compensated for by the positive effect given by its high surface area. This reinforces the notion that the surface area was not entirely responsible for the high activity. The lower activity of Mo_2C/C prepared at 900 °C and 1000 °C could presumably be attributed to sintering of particles, as indicated by the significant drop in the BET area of the composite.

Since catalyst loading on the electrodes is an important factor to take into account in determining the current density, its effect was studied and the results are shown in Fig. 5B. The current density increased monotonically with the increase in loading from 0.25 to 1.0 mg cm^{-2}. However, a further increase in the catalyst loading, such as 1.5 and 2.0 mg cm^{-2}, resulted in a decrease in current density. An increase in the current density could presumably be rationalized in terms of an increased number of active sites. Similar activity behavior with respect to catalyst loading is reported elsewhere.[10] It is most likely that such a behavior has a direct relationship with mass transport through the thin-film electrode. In our case, it seems that loadings higher than 1 mg cm^{-2} can cause a mass transport limitation; be it diffusion of electrolyte or release of hydrogen from active sites in the thin-film electrode. Thickness of the electrode depends on density of materials (Mo_2C/C) and loading as well.

Since the catalyst prepared at 800 °C with 1 mg cm^{-2} loading showed the best electrocatalytic activity towards H_2 evolution reaction, its performance was compared with that of the commercial electrocatalyst Pt/C. Furthermore, to perceive the significance of using a metal–organic framework as a source of carbon and support, Mo_2C supported on high surface area carbon black (XC72R) was also synthesized under identical synthesis conditions (800 °C, 2 h) and its activity was also compared. The comparative electrocatalytic study was carried out under identical experimental conditions with the same mass of catalyst loading on the GC electrode (Fig. 5C). As could be seen, for 10 mA current density, the required potentials for Pt/C, Mo_2C/C and Mo_2C/XC72 were recorded to be ~57, 165 and 229 mV, respectively. As expected, Pt/C electrocatalyst still showed the best performance, followed by the as-prepared catalyst Mo_2C/C and Mo_2C/XC72. In virtue of the unique metal–support interaction presumably owing to smaller particle size with fair dispersion, Mo_2C/C exhibited excellent electrocatalytic activity for HER in alkaline media. Moreover, the Tafel plots, presented in Fig. 5D, showed a fairly low Tafel slope of 63.6 mV per decade for Mo_2C/C, higher than 55.7 mV per decade for the Pt/C but lower than 74.5 mV per decade for the Mo_2C/XC72.

To investigate the durability of as-prepared electrocatalyst, the experiment was conducted under identical conditions, but at constant potential (165 mV) for 20 h. Fig. 5E shows the change in current density with respect to time. As observed, the drop in current density was insignificant after 20 h demonstrating the stability of Mo_2C/C under the applied experimental conditions. Furthermore, after 20 h of reaction, the used electrode was re-polarized and the current density was quantified as a function of potential. The comparative polarization curves recorded before and after the potential hold test are shown in Fig. 5F. It was noticed that the overvoltage corresponding to current density of 10 mA cm^{-2} had increased by 20 mV. It is known, however, that metal carbides in aqueous solutions can passivate and form oxycarbide layer on the surface and this may contribute in enhancing the electrical resistance in the thin-film electrode. More investigation is underway to better understand the loss in HER activity after holding the potential at 165 mV.

Further kinetic insights about electrode process and charge transfer was obtained by electrochemical impedance spectroscopy (EIS) studies. All the measurements were conducted from 10^5 Hz to 0.01 Hz with an AC amplitude of 10 mV at different overpotentials (η = 0 to 200 mV *vs.* NHE) in alkaline solution of 1.0 M KOH. A representative Nyquist plot of Mo_2C/C as a function of electrode overpotential is shown in Fig. 6A. The plot indicated the existence of two semicircles, an enlarged view is presented in Fig. 6B, at all applied overpotentials. A typical Bode plot, depicted in Fig. 6C, further confirms the presence of two-time constants in the catalyst system. In the reported investigations, EIS results for hydrogen evolution reaction have been predominantly construed by three types of electrical equivalent circuit models; one-time constant model,[54] two-time constant parallel model[8,55] and two time constant serial models.[56] In this study, the two-time constant parallel model, which consists of solution resistance (R_s) in series with two parallel constant phase element-resistance, was exercised to fit the experimental data (inset figure in Fig. 6A). According to this model, R_s represents a collective resistance which, includes the resistance coming from wiring (R_{wiring}), carbon support (R_{carbon}), resistance of Mo_2C ($R_{carbide}$), and the solution resistance (R_{soln}).[57] The semicircle observed at higher frequency could be attributed to the surface porosity (corroborates BET observation), whereas

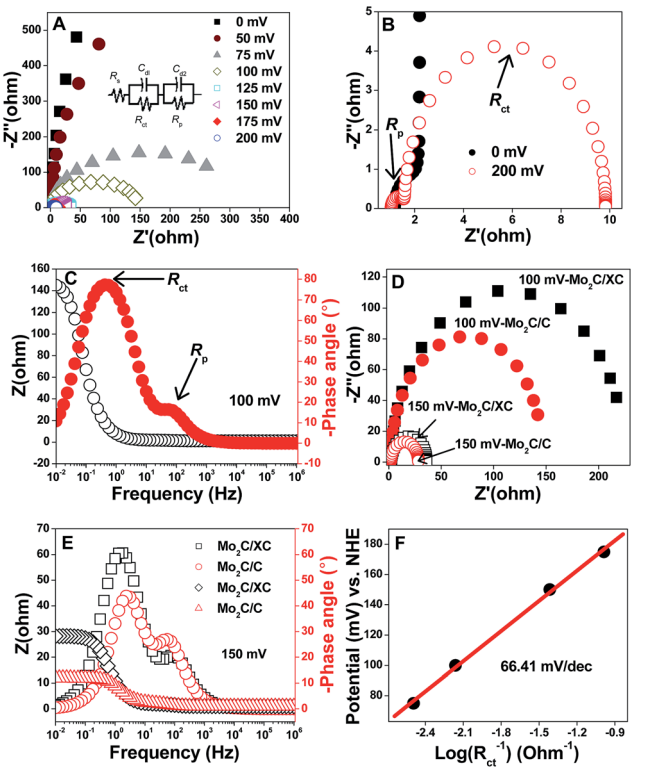

Fig. 6 Nyquist plots recorded at different potential (*vs.* NHE) (A), Nyquist plots with enlarged region showing two semicircles (B), Bode plots showing two two-time constants (C), comparative Nyquist plots of Mo_2C/C and Mo_2C/XC at η = 100 mV and 150 mV (D), comparative Bode plots of Mo_2C/C and Mo_2C/XC at η = 100 mV (E), and Tafel plot (F). Inset figure in (A) – electrical equivalent circuit model used to fit the EIS results (also in Fig. S9†).

the other semicircle at lower frequency corresponds to the charge transfer process of the hydrogen evolution reaction.[57] These results demonstrated significant dependency on the charge transfer process on the applied potential; charge transfer resistance (R_{ct}) decreased with increasing overpotential suggesting faster charge transfer kinetics at high overpotential. R_{ct} values decreased noticeably from 145 Ω at 100 mV to 8 Ω at 200 mV overpotential. A comparative EIS response of Mo_2C/C and Mo_2C/XC at 100 and 150 mV overpotentials are depicted in Fig. 6D. Moreover, a comparative analysis of Z (Ω) and phase angle as a function of frequency is illustrated in Fig. 6E. Nyquist plots of Mo_2C/XC also revealed the presence of two time constants as could be clearly seen in the Bode plots presented in Fig. 6E. The existence of two-time constants in Mo_2C/XC catalyst was also found in a previous investigation.[8] The results shown in Fig. 6D and E suggested faster charge transfer kinetics on the Mo_2C/C surface as compared to Mo_2C/XC; the R_{ct} for Mo_2C/XC and Mo_2C/C were 34.5 Ω and 24.6 Ω, respectively at $\eta = 150$ mV. This could presumably be attributed to the mesoporous surface of MOF-derived carbon in Mo_2C/C, which could render faster desorption of H_2 from active surface sites following Volmer–Heyrovsky mechanism as discussed below.

The Tafel analysis of the polarization curve suggested the operative mechanism in the HER reaction.[8,11,17] However, the selection of the actual region of the polarization curve could result in ambiguous interpretation of the Tafel slope and consequently the HER mechanism. Hence, EIS measurements were conducted to deduce the Tafel slopes and further compared to those derived from polarization curves (linear voltammetry). Computation of the semi-logarithmic values of the inverse of R_{ct} against η resulted in a linear relationship with a gradient, which corresponds to the Tafel slope of 66.41 mV dec^{-1} (Fig. 6F). The Tafel slope results obtained from the polarization curve and EIS data were almost analogous. Such Tafel slopes reveal that HER on the as-synthesized Mo_2C/C using this new approach follows the Volmer–Heyrovsky mechanism and the rate determining step could be the step III, which is electrochemical desorption as depicted below:

Step I: $H_2O + e \rightarrow H_{ads} + OH^-$ Volmer reaction (adsorption)

Step II: $H_{ads} + H_{ads} \rightarrow H_2$ Tafel reaction (chemical desorption)

Step III: $H_2O + H_{ads} + e \rightarrow$
$H_2 + OH^-$ Heyrovsky reaction (electrochemical desorption)

Conclusions

In summary, we demonstrated a novel strategy to prepare β-Mo_2C supported on mesoporous carbon for the H_2 evolution reaction. In this approach, a metal–organic framework, namely MIL-53(Al), rendered (1) confined environment for the nucleation and growth of fine Mo_2C nanoparticles and (2) porous and rigid support for Mo_2C nanoparticles. Restricted space in the form of porous texture of MIL 53(Al) appeared to inhibit agglomeration and coalescence of *in situ*-developed Mo_2C, presumably through homogeneous distribution of molybdenum on the outer and inner frameworks of MOF, and thus guided the formation of fine (5–10 nm) and fairly dispersed Mo_2C nanocrystallites in the carbon texture. The as-synthesized Mo_2C/C heterostructure showed highly efficient electrocatalytic hydrogen evolution in alkaline aqueous media; better than that of Mo_2C/XC72 and close to commercial electrocatalyst Pt/C. Electrochemical impedance analysis of Mo_2C/C suggested the presence of two-time constants and the improved electrocatalytic performance of Mo_2C/C was attributed to faster charge kinetics. Furthermore, Tafel slope suggested that a Volmer–Heyrovsky mechanism was operative in the HER reaction. This impregnation method, demonstrated by the preparation of Mo_2C-based electrocatalyst, could open new avenues for developing a variety of nanostructured catalysts using the porous texture of metal–organic frameworks.

Acknowledgements

The authors acknowledge the financial support provided by Saudi Aramco through the EXPEC Advanced Research Center for funding this work through project no.: CENT-2203 at King Fahd University of Petroleum and Minerals, KFUPM.

Notes and references

1 Q. Lu, G. S. Hutchings, W. Yu, Y. Zhou, R. V. Forest, R. Tao, J. Rosen, B. T. Yonemoto, Z. Cao, H. Zheng, J. Q. Xiao, F. Jiao and J. G. Chen, *Nat. Commun.*, 2015, **6**, 6567–6574.
2 M. S. Fabera and S. Jin, *Energy Environ. Sci.*, 2014, **7**, 3519–3542.
3 P. Xiao, W. Chen and X. Wang, *Adv. Energy Mater.*, 2015, **5**, 1500985–1500997.
4 P. C. K. Vesborg, B. Seger and I. Chorkendorff, *J. Phys. Chem. Lett.*, 2015, **6**, 951–957.
5 V. R. Stamenkovic, B. Fowler, B. S. Mun, G. Wang, P. N. Ross, C. A. Lucas and N. M. Marković, *Science*, 2007, **315**(5811), 493–497.
6 E. J. Popczun, J. R. McKone, C. G. Read, A. J. Biacchi, A. M. Wiltrout, N. S. Lewis and R. E. Schaak, *J. Am. Chem. Soc.*, 2013, **135**, 9267–9270.
7 P. D. Tran, S. Y. Chiam, P. P. Boix, Y. Ren, S. S. Pramana, J. Fize, V. Artero and J. Barber, *Energy Environ. Sci.*, 2013, **6**, 2452–2459.
8 W. F. Chen, C. H. Wang, K. Sasaki, N. Marinkovic, W. Xu, J. T. Muckerman and Y. Z. R. R. Adzicm, *Energy Environ. Sci.*, 2013, **6**, 943–951.
9 H. B. Wu, B. Y. Xia, L. Yu, X. Y. Yu and X. W. D. Lou, *Nat. Commun*, 2015, **6**, 6512.
10 C. He and J. Tao, *Chem. Commun.*, 2015, **51**, 8323–8325.
11 W. F. Chen, J. T. Muckerman and E. Fujita, *Chem. Commun.*, 2013, **49**, 8896–8909.
12 L. F. Pan, Y. H. Li, S. Yang, P. F. Liu, M. Q. Yua and H. G. Yang, *Chem. Commun.*, 2014, **50**, 13135–13137.
13 S. Meyerb, A. V. Nikiforova, I. M. Petrushinaa, K. Köhlerb, E. Christensena, J. O. Jensena and N. J. Bjerrum, *Int. J. Hydrogen Energy*, 2015, **40**, 2905–2911.
14 X. Fan, H. Zhou and X. Guo, *ACS Nano*, 2015, **9**, 5125–5134.

15 J. F. Lin, O. Pitkänen, J. Mäklin, R. Puskas, A. Kukovecz, A. Dombovari, G. Toth and K. Kordas, *J. Mater. Chem. A*, 2015, **3**, 14609–14616.
16 D. J. Li, U. N. Maiti, J. Lim, D. S. Choi, W. J. Lee, Y. Oh, G. Y. Lee and S. O. Kim, *Nano Lett.*, 2014, **14**, 1228–1233.
17 C. G. Morales-Guio, L. A. Stern and X. Hu, *Chem. Soc. Rev.*, 2014, **43**, 6555–6569.
18 D. Voiry, H. Yamaguchi, J. Li, R. Silva, D. C. Alves, T. Fujita, M. Chen, T. Asefa, V. B. Shenoy, G. Eda and M. Chhowalla, *Nat. Mater.*, 2013, **12**, 850–855.
19 S. M. Tan and M. Pumera, *ACS Appl. Mater. Interfaces*, 2016, **8**, 3948–3957.
20 D. Kong, H. Wang, Z. Lu and Y. Cui, *J. Am. Chem. Soc.*, 2014, **136**, 4897–4900.
21 A. I. Carim, F. H. Saadi, M. P. Soriaga and N. S. Lewis, *J. Mater. Chem. A*, 2014, **2**, 13835–13839.
22 X. Wang, Y. V. Kolen'ko, X. Q. Bao, K. Kovnir and L. Liu, *Angew. Chem.*, 2015, **54**, 8188–8192.
23 J. S. Moon, J. H. Jang, E. G. Kim, Y. H. Chung, S. J. Yoo and Y. K. Lee, *J. Catal.*, 2015, **326**, 92–99.
24 Z. X. Cai, X. H. Song, Y. R. Wang and X. Chen, *ChemElectroChem*, 2015, **2**, 1665–1671.
25 A. B. Laursen, K. R. Patraju, W. M. J. hitaker, M. Retuerto, T. Sarkar, N. Yao, K. V. Ramanujachary, M. Greenblatt and G. C. Dismukes, *Energy Environ. Sci.*, 2015, **8**, 1027–1034.
26 M. Ledendecker, C. S. Krick, C. Papp, H. P. Steinrück, M. Antonietti and M. Shalom, *Angew. Chem.*, 2015, **127**, 12538–12542.
27 Q. Liu, J. Tian, W. Cui, P. Jiang, N. Cheng, A. M. Asiri and X. Sun, *Angew. Chem.*, 2014, **53**, 6828–6832.
28 R. Liu, S. Gu, H. Du and C. M. Li, *J. Mater. Chem. A*, 2014, **2**, 17263–17267.
29 Y. Xu, R. Wu, J. Zhang, Y. Shi and B. Zhang, *Chem. Commun.*, 2013, **49**, 6656–6658.
30 Y. Shi and B. Zhang, *Chem. Soc. Rev.*, 2016, **45**, 1529–1541.
31 B. Cao, G. M. Veith, J. C. Neuefeind, R. R. Adzic and P. G. Khalifah, *J. Am. Chem. Soc.*, 2013, **135**, 19186–19192.
32 C. W. F. hen, K. Sasaki, C. Ma, A. I. Frenkel, N. Marinkovic, J. T. Muckerman, Y. Zhu and R. R. Adzic, *Angew. Chem.*, 2012, **51**, 6131–6135.
33 R. Wu, J. Zhang, Y. Shi, D. Liu and B. Zhang, *J. Am. Chem. Soc.*, 2015, **137**, 6983–6986.
34 R. Xu, R. Wu, Y. Shi, J. Zhang and B. Zhang, *Nano Energy*, 2016, **24**, 103–110.
35 F. A. Armstrong, N. A. Belsey, J. A. Cracknell, G. Goldet, A. Parkin, E. Reisner, K. A. Vincent and A. F. Wait, *Chem. Soc. Rev.*, 2009, **38**, 36–51.
36 L. A. Berben and J. C. Peters, *Chem. Commun.*, 2010, **46**, 398–400.
37 B. Winther-Jensen, K. Fraser, C. Ong, M. Forsyth and D. R. MacFarlane, *Adv. Mater.*, 2010, **22**, 1727–1730.
38 T. F. Jaramillo, K. P. Jørgensen, J. Bonde, J. H. Nielsen, S. Horch and I. Chorkendorff, *Science*, 2007, **317**, 100–102.
39 A. L. Goff, V. Artero, B. Jousselme, P. D. Tran, N. Guillet, R. Métayé, A. Fihri, S. Palacin and M. Fontecave, *Science*, 2009, **326**, 1384–1387.
40 P. D. Tran, A. L. Goff, J. Heidkamp, B. Jousselme, N. Guillet, S. Palacin, H. Dau, M. Fontecave and V. Artero, *Angew. Chem., Int. Ed.*, 2011, **50**, 1371–1374.
41 N. S. Alhajri, D. H. Anjum and K. Takanabe, *J. Mater. Chem. A*, 2014, **2**, 10548–10556.
42 K. Zhang, C. Li, Y. Zhao, X. Yu and Y. Chen, *Phys. Chem. Chem. Phys.*, 2015, **17**, 16609–16614.
43 Z. Shi, Y. Wang, H. Lin, H. Zhang, M. Shen, S. Xie, Y. Zhang, Q. Gao and Y. Tang, *J. Mater. Chem. A*, 2016, **4**, 6006–6013.
44 X. L. Fan, P. F. Liu, X. Yan, L. Gu, Z. Z. Yang, H. G. Yang, S. Qiu and X. Yao, *Nat. Commun.*, 2016, **7**, 10667–10673.
45 N. A. Khan, J. W. Jun, J. H. Jeong and S. H. Jhung, *Chem. Commun.*, 2011, **47**, 1306–1308.
46 J. Liu, F. Zhang, X. Zou, G. Yu, N. Zhao, F. Fan and G. Zhu, *Chem. Commun.*, 2013, **49**, 7430–7432.
47 C. Wan, Y. N. Regmi and B. M. Leonard, *Angew. Chem., Int. Ed.*, 2014, **53**, 6407–6410.
48 Y. Zhang, Q. Gao, Z. Lin, T. Zhang, J. Xu, Y. Tan, W. Tian and L. Jiang, *Sci. Rep.*, 2014, **4**, 4947–4952.
49 H. Vrubel, D. Merki and X. Hu, *Energy Environ. Sci.*, 2012, **5**, 6136–6144.
50 J. Kibsgaard, Z. Chen, B. N. Reinecke and T. F. Jaramillo, *Nat. Mater.*, 2012, **11**, 963–969.
51 F. Safizadeh, E. Ghali and G. Houlachi, *Int. J. Hydrogen Energy*, 2015, **40**, 256–274.
52 H. Ang, H. Wang, B. Li, Y. Zong, X. Wang and Q. Yan, *Small*, 2016, **12**, 2859–2865.
53 T. Y. Ma, S. Dai, M. Jaroniec and S. Z. Qiao, *J. Am. Chem. Soc.*, 2014, **136**, 13925–13931.
54 X. Yan, L. Tian, M. He and X. Chen, *Nano Lett.*, 2015, **15**, 6015–6021.
55 L. Liao, S. Wang, J. Xiao, X. Bian, Y. Zhang, M. D. Scanlon, X. Hu, Y. Tang, B. Liu and H. H. Girault b, *Energy Environ. Sci.*, 2014, **7**, 387–392.
56 A. R. J. Kucernak and V. N. N. Sundaram, *J. Mater. Chem. A*, 2014, **2**, 17435–17445.
57 W. Cui, C. Ge, Z. Xing, A. M. Asiri and X. Sun, *Electrochim. Acta*, 2014, **137**, 504–510.

